Time-Domain Absorbing Boundary Terminations for Waveguide Ports Based on State-Space Models

Thomas Flisgen, Johann Heller, and Ursula van Rienen

Universität Rostock, IEF, IAE, Rostock 18059, Germany

Absorbing boundary conditions for waveguide ports in time domain are important elements of transient approaches to treat RF structures. A successful way to implement these termination conditions is the decomposition of the transient fields in the absorbing plane in terms of modal field patterns. The absorbing condition is then accomplished by transferring the wave impedances (or admittances) of the modes to time domain, which leads to convolution operations involving Bessel functions and integrals of Bessel functions. This paper presents a new alternative approach: the convolution operations are approximated by appropriate state-space models whose system responses can be conveniently computed by standard integration schemes. These schemes are indispensable for transient simulations anyhow. Sufficiently far away from the cutoff frequency, a wideband match is achieved.

Index Terms—**Modal analysis, modal wave absorption, time-domain analysis, waveguide boundary condition.**

I. Introduction

THE investigation of closed RF structures with open waveguide ports in time domain is a standard task in computational electromagnetics. Often, for this purpose, boundary conditions at the waveguide ports are required ensuring that waves incident on the ports from inside of the RF structure are not scattered back into the structure. In the literature, a large variety of methods (see [1]–[3]) is discussed to tackle this problem. This paper presents a new approach to construct multimodal waveguide port boundary termination conditions for time-domain computations employing state-space models (SSMs). The presented method is based on the transform of the well-known characteristic admittances of port modes in frequency domain to time domain, as it is proposed in [4] and [5]. However, in contrast to [4] and [5], the presented modal absorbing boundary condition (MABC) does not require to evaluate convolution integrals involving Bessel functions. Instead, the convolution operations are approximated by suitable SSMs, whose system responses are conveniently computable by means of standard integration schemes. This is a key benefit of this approach since such integration schemes are a central element of time-domain simulations. The method can be easily implemented and employed for arbitrary waveguide cross sections. It works below and above the cutoff frequencies of the waveguide modes. Moreover, it is a suitable formalism to match waveguide ports of compact time-domain models [6] because fields are solely needed in one port plane.

II. General Theory

To convey the basic idea for the proposed termination condition, a waveguide port that is connected to an RF structure via a short waveguide with constant cross section is shown in Fig. 1(a). Facet $\partial\Omega_{\mathrm{wg}}$ (gray area) denotes the absorbing waveguide boundary. Ideally, waves traveling from the RF structure toward the absorbing boundary are not reflected. It is commonly known that the transient transverse electric and magnetic fields in the plane $\partial\Omega_{\mathrm{wg}}$ which is enclosed by perfect electric conducting (PEC) walls, can be described by means of frequency- and time-independent orthonormalized mode patterns $\mathbf{L}_{\mathrm{t},m}(\mathbf{r}_t)$

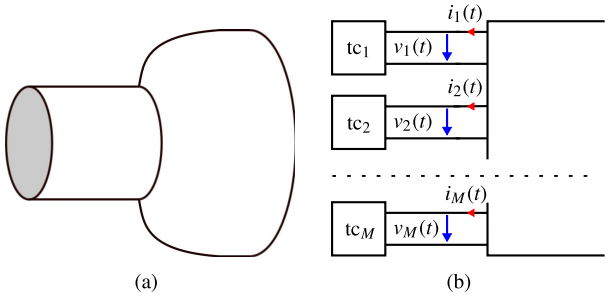

Fig. 1. (a) Waveguide port (not necessarily circular, but homogeneously filled) connected to a suggested 3-D RF structure. The gray facet shows the absorbing waveguide boundary $\partial\Omega_{\mathrm{wg}}$. (b) Equivalent circuit of the waveguide boundary, where only M (of an infinite number of) port modes are shown by their modal terminal voltages $v_m(t)$ and currents $i_m(t)$. The blocks accounting for the termination conditions (tc$_m$) are connected to the terminals.

$$\mathbf{E}_{\mathrm{t}}(\mathbf{r}_{\mathrm{t}}, t) = \sum_{m=1}^{\infty} \mathbf{L}_{\mathrm{t},m}(\mathbf{r}_{\mathrm{t}})\, v_m(\mathrm{t}) \tag{1}$$

$$\mathbf{H}_{\mathrm{t}}(\mathbf{r}_{\mathrm{t}}, t) = \sum_{m=1}^{\infty} \mathbf{n}_z \times \mathbf{L}_{\mathrm{t},m}(\mathbf{r}_{\mathrm{t}})\, i_m(\mathrm{t}) \tag{2}$$

where $v_m(t)$ and $i_m(t)$ are referred to as modal voltages and currents and $\mathbf{n}_z$ is the normal vector of $\partial\Omega_{\mathrm{wg}}$ pointing out of the structure. The transverse spatial coordinates are denoted by $\mathbf{r}_{\mathrm{t}} \in \partial\Omega_{\mathrm{wg}}$. The patterns $\mathbf{L}_{\mathrm{t},m}(\mathbf{r}_{\mathrm{t}})$ are determined by solving the 2-D Helmholtz equation on $\partial\Omega_{\mathrm{wg}}$. Moreover, the patterns regard TE as well as TM waveguide modes. From (1) and (2), it is obvious that an infinite number of modes is needed for the field construction. However, only a finite number of modes with cutoff frequency ω_{co} in or below the frequency interval of interest can principally propagate through the waveguide of constant cross section, which is shown in Fig. 1(a). The remaining modes are evanescent modes with cutoff frequency ω_{co} above the frequency interval of interest. These modes exponentially decay along the waveguide with decay rate depending on ω_{co}. Thus, all the modes above cutoff and only the first set of modes below cutoff need to be considered in (1) and (2). Therefore, it is sufficient to employ only this finite

Manuscript received June 28, 2013; revised August 16, 2013; accepted September 18, 2013. Date of current version February 21, 2014. Corresponding author: T. Flisgen (e-mail: thomas.flisgen@uni-rostock.de).

Color versions of one or more of the figures in this paper are available online at http://ieeexplore.ieee.org.

Digital Object Identifier 10.1109/TMAG.2013.2283065

number of accessible modes [4, p. 476] for the transverse field expansion. Fig. 1(b) shows the equivalent circuit for the waveguide port. M mode patterns and their respective transient modal voltages $v_m(t)$ and currents $i_m(t)$ are shown. The exact infinite guide [4, p. 476] modal termination conditions (tc_m) for voltages and currents are well-known in frequency domain

$$I_m(s) = Z_{0,m}^{-1}(s)\; V_m(s) = G_{0,m}(s)\; V_m(s) \tag{3}$$

where $s = j\omega$ is the complex angular frequency and $V_m(s)$ and $I_m(s)$ are the complex modal voltages and currents of the mth mode in frequency domain. $Z_{0,m}(s)$ and $G_{0,m}(s)$ denote the modal characteristic wave impedances and admittances of the mth port mode. Relation (3) emulates the short waveguide with constant cross section [Fig. 1(a)] to be infinitely long such that there is no reflection from $\partial\Omega_{\mathrm{wg}}$. The modal characteristic wave impedances and admittances are different for TE and TM port modes (see [4], [5], and [7])

$$G_{0,m}^{\mathrm{TE}}(s) = \frac{1}{Z_{0,m}^{\mathrm{TE}}(s)} = \frac{1}{\eta}\;\psi^{-1}\!\left(\frac{s}{\omega_{\mathrm{co},m}}\right) \tag{4}$$

$$G_{0,m}^{\mathrm{TM}}(s) = \frac{1}{Z_{0,m}^{\mathrm{TM}}(s)} = \frac{1}{\eta}\;\psi\!\left(\frac{s}{\omega_{\mathrm{co},m}}\right) \tag{5}$$

with the nonrational function

$$\psi(\tilde{s}) = \frac{\tilde{s}}{\sqrt{\tilde{s}^2+1}}. \tag{6}$$

In (4) and (5), $\omega_{\mathrm{co},m}$ denotes the cutoff frequency of the mth mode and $\eta = \sqrt{\mu/\varepsilon}$ is the wave impedance of the homogeneous insulator in the waveguide with the permittivity ε and the permeability μ. The transient electric field distribution of each mode at the termination corresponds to a transient magnetic field which has to be assigned by means of a surface current (see [6, Sec. II-A, eq. (15)]) in the plane $\partial\Omega_{\mathrm{wg}}$ to accomplish the absorbing condition. Therefore, (3) is transformed into time domain. The employment of the inverse Laplace transforms of (4) and (5) yields the following convolution integrals for TE and TM cases, respectively [4], [5], [7]:

$$i_m^{\mathrm{TE}}(t) = \frac{1}{\eta}\Bigg[v_m^{\mathrm{TE}}(t) + \omega_{\mathrm{co},m}\int_0^t \big(\hat{J}_0(\omega_{\mathrm{co},m}\tau) - J_1(\omega_{\mathrm{co},m}\tau)\big)\; v_m^{\mathrm{TE}}(t-\tau)\;\mathrm{d}\tau\Bigg] \tag{7}$$

and

$$i_m^{\mathrm{TM}}(t) = \frac{1}{\eta}\Bigg[v_m^{\mathrm{TM}}(t) - \omega_{\mathrm{co},m}\int_0^t J_1(\omega_{\mathrm{co},m}\tau)\, v_m^{\mathrm{TM}}(t-\tau)\,\mathrm{d}\tau\Bigg]. \tag{8}$$

Here, $J_1(t)$ is the first-order Bessel function of the first kind and $\hat{J}_0(t)$ is the integral of the zeroth-order Bessel function of the first kind

$$\hat{J}_0(t) = \int_0^t J_0(u)\,\mathrm{d}u. \tag{9}$$

The convolution integrals in (7) and (8) assume that the excitation $v_m(t)$ is equal to zero for $t < 0$. One drawback of numerically evaluating the convolution integrals (e.g., by applying the midpoint rule) is the $\mathcal{O}(N_{\mathrm{ts}}^2)$ scaling of the numerical effort, where N_{ts} is the total number of time samples. Moreover, Bessel functions and integrals of Bessel functions are involved in the integrands. Alternatively, as it is shown below, the currents $i_m(t)$, which are dependent on the voltages $v_m(t)$ can be approximated by a SSM

$$\frac{\partial}{\partial t}\mathbf{x}(t) = \omega_{\mathrm{co},m}\,\mathbf{A}\,\mathbf{x}(t) + \sqrt{\frac{\omega_{\mathrm{co},m}}{\eta}}\,\mathbf{B}\,v_m(t) \tag{10}$$

$$i_m(t) = \sqrt{\frac{\omega_{\mathrm{co},m}}{\eta}}\,\mathbf{C}\,\mathbf{x}(t) + \frac{1}{\eta}\mathbf{D}\,v_m(t) \tag{11}$$

in combination with standard integration schemes, which are needed anyhow for transient simulations. Thereby, the numerical effort to evaluate the approximated $i_m(t)$ scales with $\mathcal{O}(N_{\mathrm{ts}})$. Two different sets of SSMs need to be constructed: one set $\mathrm{SSM}^{\mathrm{TE}} = \{\mathbf{A}^{\mathrm{TE}}, \mathbf{B}^{\mathrm{TE}}, \mathbf{C}^{\mathrm{TE}}, \mathbf{D}^{\mathrm{TE}}\}$ for TE modes and one set $\mathrm{SSM}^{\mathrm{TM}} = \{\mathbf{A}^{\mathrm{TM}}, \mathbf{B}^{\mathrm{TM}}, \mathbf{C}^{\mathrm{TM}}, \mathbf{D}^{\mathrm{TM}}\}$ for TM modes, respectively. These matrices are created by approximating the nonrational part of the modal characteristic admittances using a rational function, i.e., $\psi(\tilde{s}) \approx \psi_{\mathrm{rat}}(\tilde{s})$, where

$$\psi_{\mathrm{rat}}(\tilde{s}) = \frac{p_0 + p_1\tilde{s} + \cdots + p_N\tilde{s}^N}{q_0 + q_1\tilde{s} + \cdots + q_N\tilde{s}^N}. \tag{12}$$

Tests have shown that the application of a Padé approximation of $\psi(\tilde{s})$ about the point $\tilde{s} = 1$ is a reasonable way to determine the coefficients p_n and q_n. Once these coefficients are known, the state matrices are constructed according to

$$\mathbf{A} = \begin{pmatrix} 0 & a_2 & 0 & \dots & 0 \\ 0 & 0 & a_3 & & 0 \\ \vdots & \vdots & & \ddots & \\ 0 & 0 & 0 & & a_N \\ -a_1 & -a_2 & -a_3 & \dots & -a_N \end{pmatrix} \in \mathbb{R}^{N\times N} \tag{13}$$

$$\mathbf{B} = \begin{pmatrix} 0\; 0\; \dots\; 0\; 1 \end{pmatrix}^{\mathrm{T}} \in \mathbb{R}^{N\times 1} \tag{14}$$

$$\mathbf{C} = \begin{pmatrix} c_1\; c_2\; c_3 \dots\; c_N \end{pmatrix} \in \mathbb{R}^{1\times N} \tag{15}$$

$$\mathbf{D} = d \in \mathbb{R}^{1\times 1}. \tag{16}$$

For the TM case, the involved coefficients are defined by $a_n^{\mathrm{TM}} = q_{n-1}/q_n$, $c_n^{\mathrm{TM}} = p_{n-1}/q_n - (p_N\, q_{n-1})/(q_N\, q_n)$, and $d^{\mathrm{TM}} = p_N/q_N$. It follows from the proposed setup that the frequency-domain transfer function of the state-space system constituted by (13)–(16) equals the rational function

$$\psi_{\mathrm{rat}}(\tilde{s}) = \mathbf{C}^{\mathrm{TM}}\big(\tilde{s}\,\mathbf{I} - \mathbf{A}^{\mathrm{TM}}\big)^{-1}\mathbf{B}^{\mathrm{TM}} + \mathbf{D}^{\mathrm{TM}}. \tag{17}$$

For the TE case, it is obvious from (4) that the inverse of $\psi(\tilde{s})$ is needed. Therefore, its approximation $\psi_{\mathrm{rat}}(\tilde{s})$ has to be inverted as well. The inversion of this fraction is easily accomplished by exchanging all p_n with all q_n and vice versa [see (12)]. Therefore, the state matrices for the TE case are constructed in accordance with (13)–(16), but with coefficients exchanged: $a_n^{\mathrm{TE}} = p_{n-1}/p_n$, $c_n^{\mathrm{TE}} = q_{n-1}/p_n - (q_N\, p_{n-1})/(p_N\, p_n)$, and $d^{\mathrm{TE}} = q_N/p_N$. As a matter of fact, the matrices $\mathbf{A}$, $\mathbf{B}$, $\mathbf{C}$, and $\mathbf{D}$ for the TE and the TM case neither depend on the material parameters nor on the cutoff frequency. These properties are accounted for in the matrix scaling factors in (10) and (11). Basically, it is therefore sufficient to perform the Padé approximation only once. Then, the resulting state matrices can be conveniently stored in the computer code in the form of a table.

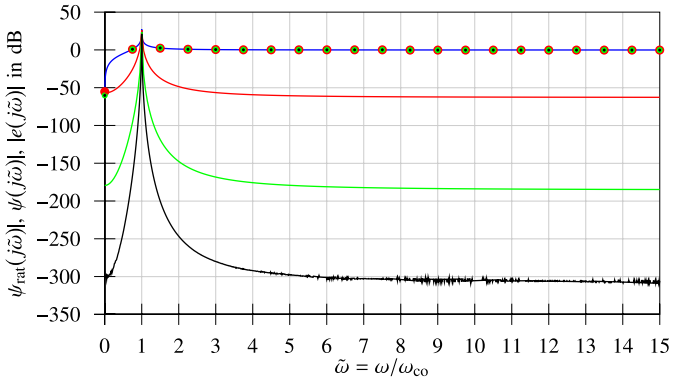

Fig. 2. Logarithmic plot of the magnitude of $\psi(j\tilde{\omega})$ (solid blue line) and its approximations $\psi_{\mathrm{rat}}(j\tilde{\omega})$ for different N (red dots: $N = 4$, green dots: $N = 12$, and black dots: $N = 20$). The absolute values $|e(j\tilde{\omega})|$ of the differences between both are shown as solid red line for $N = 4$, solid green line for $N = 12$, and solid black line for $N = 20$.

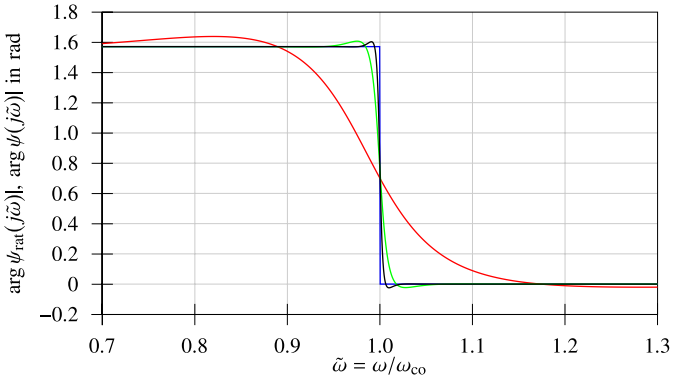

Fig. 3. Phase response of $\psi(j\tilde{\omega})$ (solid blue line) and phase response of the approximations $\psi_{\mathrm{rat}}(j\tilde{\omega})$ for different N (red $N = 4$, green $N = 12$, and black $N = 20$). The responses of the approximation are trying to follow the discrete transition of arg $\psi(j\tilde{\omega})$ of at $\tilde{\omega} = 1$.

III. Numerical Validation

For the sake of brevity, the presented validation is restricted in this section to the TM case (all validations have been performed for the TE case as well). The Padé approximations have been conducted analytically by means of [8].

A. Numerical Validation in Frequency Domain

Fig. 2 shows a frequency-domain comparison between $\psi(j\tilde{\omega})$ (solid blue line) and its rational approximations $\psi_{\mathrm{rat}}(j\tilde{\omega})$ for different N (red dots: $N = 4$, green dots: $N = 12$, and black dots: $N = 20$), where $\tilde{\omega} = \omega/\omega_{\mathrm{co},m}$. Already for $N = 4$, the curves are hard to distinguish. Therefore, the absolute values of the differences $e(j\tilde{\omega}) = \psi(j\tilde{\omega}) - \psi_{\mathrm{rat}}(j\tilde{\omega})$ are shown as solid red ($N = 4$), solid green ($N = 12$), and solid black ($N = 20$) lines. Sufficiently far away from the cutoff frequency, the difference drops below -300 dB (order of numerical noise) for $N = 20$. However, the approximation near the cutoff frequency remains poor. To explain this behavior, the phase responses close to $\tilde{\omega} = 1$ of $\psi(j\tilde{\omega})$ and $\psi_{\mathrm{rat}}(j\tilde{\omega})$ are shown in Fig. 3 for different N. Due to the nonrational characteristic of $\psi(j\tilde{\omega})$ (blue curve), the phase response shows a discrete transition from $\pi/2$ rad (real part is zero) to 0 rad (imaginary part is zero) at $\tilde{\omega} = 1$. The rational approximations $\psi_{\mathrm{rat}}(j\tilde{\omega})$ are trying to follow the discrete change.

B. Numerical Validation in Time Domain

To validate the proposed method in time domain, the normalized currents $i_m^{\mathrm{TM}}(t)\ \eta/V_0$ arising from the convolution integral (8) for $\omega_{\mathrm{co},m} = 1\,\mathrm{sec}^{-1}$ are considered. The Heaviside step function $\theta(t)$ is chosen as excitation signal, i.e., $v_m^{\mathrm{TM}}(t) = V_0\,\theta(t)$, where V_0 is a constant voltage. Three different methods to evaluate $i_m^{\mathrm{TM}}(t)$ on $N_{\mathrm{ts}} = 1000$ equidistant time samples in the interval $t = 0 \ldots 100$ sec are applied. First, an adaptive Simpson quadrature built in [9] with the absolute error tolerance of 10^{-10} is used to determine (8) ($T_{\mathrm{comp}} \approx 120$ sec). Second, the midpoint rule is employed to compute (8) ($T_{\mathrm{comp}} \approx 0.0156$ sec). Third, routines of [9] are used to calculate (10) and (11) for different N ($T_{\mathrm{comp}} \leq 0.0415$ sec). All computing times T_{comp} refer to an Intel Core 2 Duo @ 2.00 GHz machine equipped with a RAM size of 2 GB. Fig. 4 shows the resulting step responses. The blue line shows the response obtained by the adaptive Simpson quadrature and the magenta line by the midpoint rule. The red, green, and black lines show the responses computed by (10) and (11) for different N. Exempted from the red curve, all curves agree very well. The maximal absolute value of the difference between the blue and the magenta line is $3.8395 \cdot 10^{-4}$, between the blue and the red is $1.035 \cdot 10^{-1}$, between the blue and the green is $7.8 \cdot 10^{-3}$, and between the blue and the black is $3.3951 \cdot 10^{-5}$. Fig. 5 shows the dependency of the runtimes on different time samples for the midpoint rule (blue) and for the proposed scheme (red). The runtime scaling of midpoint rule shows the expected $\mathcal{O}(N_{\mathrm{ts}}^2)$ behavior, whereas the runtime of the proposed MABC scheme scales with $\mathcal{O}(N_{\mathrm{ts}})$.

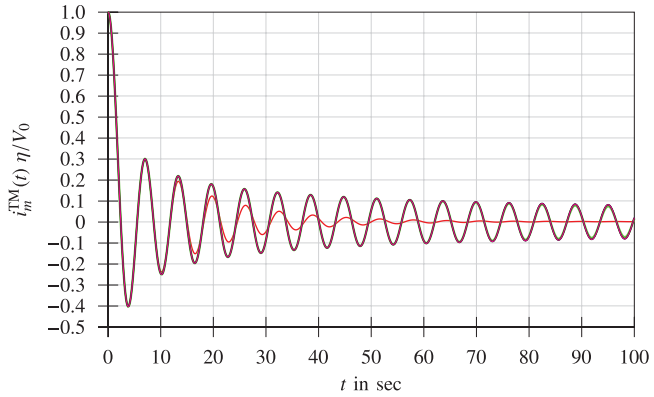

Fig. 4. Normalized step response $i_m^{\mathrm{TM}}(t)\ \eta/V_0$ for $\omega_{\mathrm{co},m} = 1\,\mathrm{sec}^{-1}$. The response is computed by means of different methods on $N_{\mathrm{ts}} = 1000$ samples. Blue: evaluation of (8) using an adaptive Simpson quadrature. Magenta: evaluation of (8) using the midpoint rule. The evaluation of (10) and (11) using an ordinary differential equation (ODE) solver is shown in red ($N = 4$), green ($N = 12$), and black ($N = 20$).

IV. Application Example

This section describes the application of the proposed MABC for a (not necessarily) lossless 3-D structure. Fig. 6(a) shows the cutaway view of a circular hollow waveguide with an antenna probe connected to a coaxial transmission line. The waveguide boundaries are highlighted with red planes. The entire structure is discretized by means of [10] using a hexahedral grid with 5000 meshcells. With this discretization one port mode $\mathbf{L}_{\mathrm{t},1}(\mathbf{r}_t)$ (TEM mode with the cutoff frequency

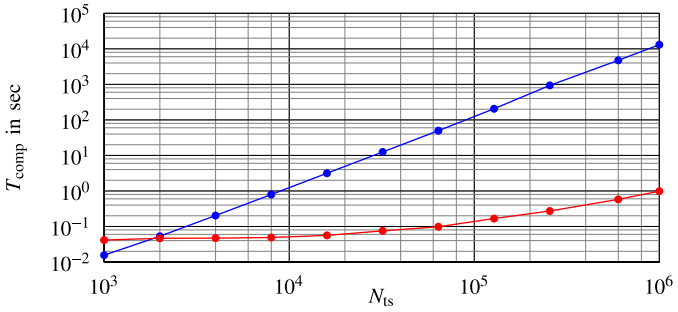

Fig. 5. Log–log graph of computational times for the application of midpoint rule (blue) and for proposed method (red) dependent on the number of time samples N_{ts}. The blue curve is proportional to N_{ts}^2, whereas the red curve is asymptotically proportional to N_{ts}.

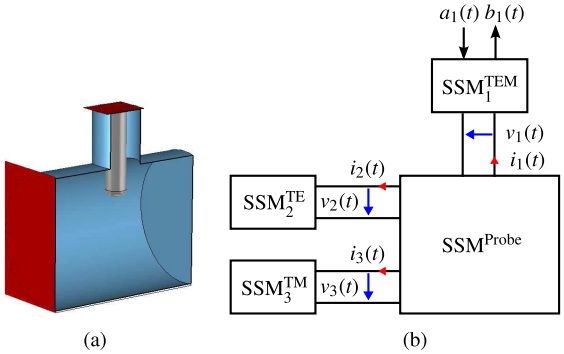

Fig. 6. (a) Cutaway view of an antenna probe protruding into a circular waveguide. Red facets: the waveguide boundaries. (b) Equivalent network of the structure, where $\text{SSM}^{\text{Probe}}$ reflects the RF properties of the 3-D structure. One port mode (TEM) is considered at the coaxial probe and two port modes (TE_{11}, TM_{01}) at the circular waveguide. The state-space models $\text{SSM}_1^{\text{TEM}}$, SSM_2^{TE}, and SSM_3^{TM} accomplish the matching of the terminals.

$f_{\text{co},1} = 0\,\text{GHz}$ and the characteristic admittance $G_{0,1}^{\text{TEM}} = 1/Z_{0,1}^{\text{TEM}} = 0.02\,\text{S}$) at the end of the coaxial transmission line and two port modes $\mathbf{L}_{\text{t},2}(\mathbf{r}_t)$ and $\mathbf{L}_{\text{t},3}(\mathbf{r}_t)$ (TE_{11} mode with $f_{\text{co},2} = 4.38\,\text{GHz}$ and TM_{01} mode with $f_{\text{co},3} = 5.73\,\text{GHz}$) at the left end of the waveguide are computed. The discretization and the port modes are employed to create the $\text{SSM}^{\text{Probe}}$ of the 3-D structure in an impedance formulation. In a following step, the matching state-space models SSM^{TE} with $\omega_{\text{co},2} = 2\,\pi\,f_{\text{co},2}$ and SSM^{TM} with $\omega_{\text{co},3} = 2\,\pi\,f_{\text{co},3}$ are connected to the terminals related to the TE and TM port modes. Therefore, the reflection from this boundary plane should vanish. In addition, the terminal related to the antenna probe is connected to an SSM, which matches the coaxial probe with its frequency-independent wave admittance $G_{0,1}^{\text{TEM}}$ and expresses the modal voltages $v_1(t)$ and currents $i_1(t)$ in terms of incident $a_1(t)$ and reflected $b_1(t)$ wave amplitudes [6, Sec. II-E]. Fig. 6(b) shows the resulting structure in terms of a block diagram. In a next step, the TEM port is excited with an incident Gaussian signal (see black curve in Fig. 7). The pulse carries rms energy in the interval $f_{\text{min}} = 1\,\text{GHz}$ to $f_{\text{max}} = 6\,\text{GHz}$, such that it is not sufficient to regard only the TE_{11} port mode as the TM_{01} port mode can propagate in this interval as well. The dashed blue curve shows the scattered wave amplitudes $b_1(t)$ computed by the transient solver of [10] directly. The red curve shows the response computed by the employment of the combined SSM with the proposed MABCs [Fig. 6(b)] and an ODE solver [9]. As a matter of fact, both curves show a very good agreement.

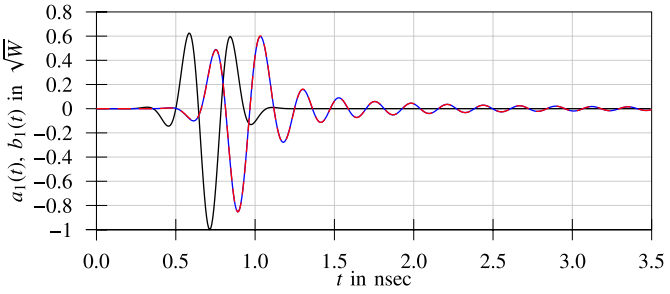

Fig. 7. Comparison of reflected wave amplitudes $b_1(t)$ [dashed blue curve computed by the transient solver of [10], red curve determined by solving the ODE arising from Fig. 6(b)] at the coaxial port of the structure shown in Fig. 6(a) due to the Gaussian excitation of $a_1(t)$ (solid black curve).

V. Conclusion

The presented MABC avoids the explicit calculation of convolution integrals with Bessel functions, which are needed to transfer the well-known reflection free termination condition for waveguide port modes to time domain. The frequency-domain validation of the MABC shows that sufficiently far away from the cutoff frequency of the port modes, the approximation error falls to the order of the numerical noise. However, the approximation at the cutoff frequency stays poor. Nonetheless, the time-domain validations demonstrate that the scheme delivers very reasonable transient signals with an $\mathcal{O}(N_{\text{ts}})$ instead of an $\mathcal{O}(N_{\text{ts}}^2)$ scaling of the numerical effort. In addition, reflected signals yielded by the employment of the proposed MABC scheme agree well with signals computed by commercial software (see [10]).

Acknowledgment

This work was supported by the EuCARD Project, co-funded by the European Commission 7th in Framework Programme.

References

[1] J.-P. Bérenger, "A perfectly matched layer for the absorption of electromagnetic waves," *J. Comput. Phys.*, vol. 114, no. 2, pp. 185–200, Oct. 1994.

[2] F. Alimenti, P. Mezzanotte, L. Roselli, and R. Sorrentino, "A revised formulation of modal absorbing and matched modal source boundary conditions for the efficient FDTD analysis of waveguide structures," *IEEE Trans. Microw. Theory Tech.*, vol. 48, no. 1, pp. 50–59, Jan. 2000.

[3] Z. Lou and J.-M. Jin, "An accurate waveguide port boundary condition for the time-domain finite-element method," *IEEE Trans. Microw. Theory Tech.*, vol. 53, no. 9, pp. 3014–2023, Sep. 2005.

[4] F. Moglie, T. Rozzi, P. Marcozzi, and A. Schiavoni, "A new termination condition for the application of FDTD techniques to discontinuity problems in close homogeneous waveguide," *IEEE Microw. Guided Wave Lett.*, vol. 2, no. 12, pp. 475–477, Dec. 1992.

[5] L. Pierantoni, C. Tomassoni, and T. Rozzi, "A new termination condition for the application of the TLM method to discontinuity problems in closed homogeneous waveguide," *IEEE Trans. Microw. Theory Tech.*, vol. 50, no. 11, pp. 2513–2518, Nov. 2002.

[6] T. Flisgen, H.-W. Glock, and U. van Rienen, "Compact time-domain models of complex RF structures based on the real eigenmodes of segments," *IEEE Trans. Microw. Theory Tech.*, vol. 61, no. 6, pp. 2282–2294, Jun. 2013.

[7] T.-H. Loh and C. Mias, "Implementation of an exact modal absorbing boundary termination condition for the application of the finite-element time-domain technique to discontinuity problems in closed homogeneous waveguides," *IEEE Trans. Microw. Theory Tech.*, vol. 52, no. 3, pp. 882–888, Mar. 2004.

[8] *Mathematica, Version 7.0*, Wolfram Research, Inc., Champaign, IL, USA, 2009.

[9] *Matlab, Version R2011b*, MathWorks, Inc., Natick, MA, USA, 2011.

[10] *CST Studio Suite, Version 2012*, CST AG, Darmstadt, Germany, 2012.